

Cite this: *RSC Advances*, 2012, **2**, 1387–1403[www.rsc.org/advances](http://www.rsc.org/advances)

PAPER

# Growth morphologies, phase formation, optical & biological responses of nanostructures of CuO and their application as cooling fluid in high energy density devices

Kajal Kumar Dey,<sup>a,c</sup> Ashutosh Kumar,<sup>b</sup> Rishi Shanker,<sup>b</sup> Alok Dhawan,<sup>b</sup> Meher Wan,<sup>c</sup> Raja Ram Yadav<sup>c</sup> and Avanish Kumar Srivastava<sup>\*a</sup>

Received 10th September 2011, Accepted 21st October 2011

DOI: 10.1039/c1ra00710f

Different nanoscale objects of CuO have been synthesized by a simple chemical route where the Cu(OH)<sub>2</sub> nanostructures were first synthesized by the alkaline hydrolysis of Cu(NO<sub>3</sub>)<sub>2</sub>·3H<sub>2</sub>O using NaOH as a base and the synthesized precipitate was subsequently annealed at a temperature of 130 °C. The alkaline content (pH) of the solutions during the hydrolysis process was varied to tailor the morphologies and dimensions of the nanostructures, consequently a series of fascinatingly shaped nanostructures, *e.g.* seeds, ellipsoidal, rods and leaves were obtained. Topographical characteristics along with the mechanism behind the structural variation have been rationalized by XRD, FTIR, SEM and HRTEM investigations. Optical performance of these samples provided simultaneous emission in the visible bands of blue, green, yellow and red, which were correlated to the size, shape and structural defects of these nano-scaled objects. The toxicity of these nanostructured materials were also put into perspective and it was found that the leaf shaped particles were the most toxic among the various shapes of nano-CuO. Finally the synthesized particles, when applied as nanofluids (water medium) showed their ability to enhance the thermal conductivity of water to a noticeable degree (above 40%) at high temperatures, even at very small concentrations, bespeaking their applicability in cooling fluids.

## Introduction

The world of nanomaterials has become an exciting challenge for physicists, chemists and material scientists. During the last two decades, a vast amount of knowledge on the synthesis and properties of various nanoparticles and nanocomposites has been gathered, with new insights and discoveries emerging on an almost daily basis.<sup>1–9</sup> Now that the expectations regarding the feasibility of the potential of these nanoparticles as 21st century functional materials are at an all time high, the technological limitations of the existing micro-devices are becoming apparent, underlining the importance of scaling down the conventional technologies by at least an order of magnitude, and nanoparticles (NPs) are perfectly suited building blocks for that. The outstanding physicochemical characteristics of these nanoparticles can be ascribed to their miniaturized size (surface area and size distribution), chemical composition (purity, crystallinity,

electronic properties, *etc.*), surface structure (surface reactivity, surface groups, inorganic or organic coatings, *etc.*), solubility, shape and aggregation. Although impressive from a physico-chemical viewpoint, the novel properties of nanomaterials raise concerns about adverse effects and potential toxicity on the biological environment, which at the cellular level includes structural arrangements that resemble nanomaterials in terms of their functionality.<sup>10–12</sup>

Transition metal oxide nanomaterials are functional materials that have pioneered advanced applications in diverse fields because of their unique features in terms of their optical, magnetic and electrical properties as well as their hardness, thermal stability and chemical resistance. Amongst the transition metal oxide nanomaterials which still exude great interest within the industrial and scientific fraternity, Cupric Oxide (CuO; known as tenorite in its mineral form) has long caught the imagination of researchers due to its typical structural lineaments and broad range of existing and potential applications. CuO is a unique monoxide amongst the 3d transition metal monoxides in that it has a square planar coordination of the Cu atom to the neighboring oxygen atoms and a monoclinic crystal structure, unlike the oxides of other 3d metals which predominantly have cubic rock salt crystal structures with an octahedral coordination. With a narrow band gap varying between 1.2–1.8 eV CuO has uses as a p-type semiconductor,<sup>13,14</sup>

<sup>a</sup>Electron and Ion Microscopy, Materials and Chemical Metrology, National Physical Laboratory, Council of Scientific and Industrial Research, Dr K. S. Krishnan Road, New Delhi, 110012, India.

E-mail: aks@nplindia.org

<sup>b</sup>Nanomaterial Toxicology group, Indian Institute of Toxicology Research, Council of Scientific and Industrial Research, M.G. Road, Lucknow, 226001, India

<sup>c</sup>Department of Physics, University of Allahabad, Allahabad, 211002, India

a heterogeneous catalyst,<sup>15–17</sup> in hazardous gas sensing,<sup>13,18,19</sup> as a crucial component in high temperature superconductors,<sup>20,21</sup> fabricating solar cells<sup>22,23</sup> and has a potentially huge application as an electrode material in Li-ion batteries.<sup>24,25</sup> Recently CuO NPs have gained significant attention for their utility in one of the most exciting new breeds for nanoparticle applications, thermal conductivity enhancers in nanofluids. These fluids are engineered by uniformly dispersing nanosized particles in a fluid and are widely tipped to be the next generation coolants and working fluids for innovative applications in industry such as energy, bio and pharmaceutical.<sup>26–29</sup>

The most significant challenges remaining in developing its potential are: i) the facile fabrication of desired structure shapes where the characteristics are more definitive and thus more suitable for property studies, or monitoring. ii) Correlating several shapes in terms of their utility with respect to developed applications and properties in order to determine the best corresponding shape for a particular application and iii) evaluation of these synthesized materials in terms of general safety and health concerns; keeping in mind the growing concerns regarding the toxic potential of the materials at the nanolevel.

Although CuO nanoparticles of multiple shapes and morphologies have previously been synthesized in various physical methods such as mechanical milling<sup>30</sup> or simply heating an elemental copper substrate at 400–700 °C,<sup>31</sup> solution phase chemical synthesis has arguably been the most effective way of synthesizing these nanoparticles with its cost effectiveness, control over morphology and excellent yield. The solution strategies employed so far include using hydrothermal method to give urchin like core-shell structures,<sup>19,32</sup> electrodeposition followed by self-catalytic growth using copper(II) salt as electrolyte producing nanofibers,<sup>33</sup> a one step solid state reaction using a surfactant<sup>34</sup> and the sol–gel method.<sup>35</sup> It is a well known fact that copper(II) oxide can be conventionally obtained by the thermal decomposition of copper salts in the solid state. For instance, nitrates, and sometimes hydroxysalts, can be decomposed to yield CuO.<sup>36</sup> However the solid state decomposition technique rarely gives the desired mastery over the shapes and grain sizes of the nanoparticles, unlike the simple solution phase decomposition technique. Decomposition of cupric hydroxide to produce CuO has been one such example. The biggest advantage of this method has been that the synthesized CuO nanoparticles follow the same morphological characteristics as its parent Cu(OH)<sub>2</sub> in nearly all the cases, so control over the cupric hydroxide nanostructures is likely to give sufficient control over the CuO nanostructures. This method has been adopted by previous researchers where a cupric salt has been hydrolyzed in an alkaline medium by the use of NaOH or KOH to yield Cu(OH)<sub>2</sub>, which has subsequently been thermally decomposed to yield CuO nanoparticles.<sup>37,38</sup> However, a detailed study of the effect of the reaction conditions such as pH and the reagents on the resultant morphological and structural features of the corresponding particles is still called for.

Herein, CuO nanostructure has been synthesized by a simple template free wet chemical solution method, the alkaline hydrolysis of a copper(II) salt followed by the thermal decomposition of the precipitated cupric base. We have varied the alkali concentration (pH) during hydrolysis and have studied its

effect on the size and shape of the corresponding nanostructured CuO particles and have rationalized the probable mechanism for the changes. Besides performing the usual morphological characterizations, we have observed the optical properties of these CuO nanoparticles. Although in the past, the magnetic and electrical properties of CuO has been thoroughly investigated,<sup>1,32,39,40</sup> its optical properties, especially the existence of different emission states remains sparsely studied<sup>41,42</sup> and only vaguely explored. In fact there is only a handful of literature available reporting the characteristic emission bands of CuO. Here we have made an attempt to see into the photoluminescence properties of CuO and suggest a rational explanation for the bands observed in conjunction with the varied morphologies and dimensions of the nanoscale CuO. In addition, we have evaluated these samples in terms of their toxicity with respect to mammalian (Chinese hamster ovary; CHO) cells and bacterial cells (*Escherichia coli*; *E. coli*) and determined the most bio-adverse of the various shapes of CuO that we have obtained. The prepared CuO nanoparticles at a very low concentration were used to generate water based nanofluids. The obtained results indicate a very impressive performance of the nanofluids in terms of their thermal conductivity increment. Both the toxicity response and nanofluid performance were subjected to evaluation with respect to the shape of the nanoparticles, which to the best of our knowledge, has not been attempted before for oxide nanoparticles.

## Experimental

### Chemicals

The chemicals Cu(NO<sub>3</sub>)<sub>2</sub>·3H<sub>2</sub>O (cupric nitrate trihydrate, 99.5%, Alfa Aesar) and NaOH (sodium hydroxide), were analytical grade and used without any further purification. Luria Bertani (LB) broth and 3-(4, 5-dimethylthiazol-2-yl)-2, 5-diphenyl tetrazolium bromide (MTT) dye were purchased from Hi-Media Pvt. Ltd. (Mumbai, India). Phosphate buffered saline (PBS; Ca<sup>2+</sup>, Mg<sup>2+</sup> free), F-12 medium, trypsin–EDTA, fetal bovine serum (FBS), antibiotic and antimycotic solution (10 000 U ml<sup>−1</sup> penicillin, 10 mg ml<sup>−1</sup> streptomycin 25 µg ml<sup>−1</sup> amphotericin B) were purchased from Life Technologies (India) Pvt. Ltd., (New Delhi, India). Propidium iodide was purchased from Sigma chemical Co. Ltd. (St. Louis, MO, USA). Cell culture plastic wares were obtained from Tarsons Products Pvt. Ltd. (Kolkata, India).

### Synthesis of the nanoparticles

**Hydrolysis of cupric nitrate salt.** In a typical synthesis procedure, 1 g of Cu(NO<sub>3</sub>)<sub>2</sub>·3H<sub>2</sub>O was dissolved in 100 ml of distilled water. It was followed by the drop-wise addition of NaOH solution (~1 M) with constant stirring till the solution attained the desired pH. A deep blue precipitate appeared. The appearance of this precipitate indicates the probable formation of Cu(OH)<sub>2</sub>. One interesting observation to note here is that as the pH was increased, the colour of the precipitate changed from greenish blue to dark blue. The precipitate was subsequently collected, filtered and washed repeatedly in de-ionized water to remove anions such as nitrate (NO<sub>3</sub><sup>−</sup>).

**Transformation of the intermediate precipitate into CuO nanostructures.** The obtained precipitate was heated at a

temperature of 130 °C for 10 h in a micro oven. The bluish precipitate of  $\text{Cu}(\text{OH})_2$  gradually turned black indicating the possible formation of  $\text{CuO}$  particles. The black coloured solid powder was collected and used for subsequent characterization.

### Sample characterization

The crystallographic phase identification and the purity of the obtained powder was carried out by X-ray diffraction (XRD, Bruker AXS D8 Advance X-ray Diffractometer) using monochromatized  $\text{Cu-K}\alpha$  radiation ( $\lambda = 1.54059 \text{ \AA}$ ) and scanning in  $2\theta$  range from 20 to 80°. The FT-IR spectra were recorded with a single beam Perkin Elmer instrument (Spectrum BX-500) FT-IR Model spectrophotometer. The morphological identification and sizes of the synthesized samples were based on the scanning electron microscopy images recorded on a Zeiss EVO MA-10 SEM equipped with an energy dispersive spectrometer (OXFORD INCA ENERGY 250), which assisted in the elemental analysis of the sample. Microstructural characterization at high magnifications and reciprocal space analysis were performed using a high resolution transmission electron microscope (HR-TEM: FEI Tecnai G2 F30 STWIN at 300 keV). The UV-Vis spectra of the samples were recorded by a JASCO UV/VIS/NIR SPECTROPHOTOMETER (model V-670) and the luminescence characteristics were investigated by photoluminescence spectroscopy using a Perkin-Elmer LS-55 luminescence spectrophotometer (Xe source).

### Toxicity measurements

**Sample preparation and characterization.** Different  $\text{CuO}$  nanoparticles (NPs) were suspended in F12 medium and probe sonicated (Sonics Vibra cell, Sonics & Material Inc., New Town, CT, USA) to make stock suspension ( $100 \mu\text{g ml}^{-1}$ ). This was characterized by dynamic light scattering (DLS) using a Zetasizer Nano-ZS equipped with a 4.0 mW, 633 nm laser (Model ZEN3600, Malvern instruments Ltd., Malvern, UK).

**Cell culture and exposure.** Chinese Hamster Ovary cell line (CHO) was obtained from National Centre for Cell Sciences, Pune, India, and cultured in F12 medium supplemented with 10% FBS, 0.2% sodium bicarbonate and 10  $\text{ml L}^{-1}$  antibiotic and antimycotic solution at 37 °C under a humidified atmosphere of 5%  $\text{CO}_2/95\%$  air. CHO cells were exposed to  $\text{CuO}$  NP suspensions for 3 and 6 h at concentrations of 1, 5, 10, 20, 30, 50 and  $100 \mu\text{g ml}^{-1}$  for cytotoxicity assays.

**Mitochondrial activity.** Mitochondrial succinate dehydrogenase activity was assessed using the MTT assay according to a modified method of Mosmann<sup>43</sup> described earlier by Shukla *et al.*<sup>44</sup> Briefly, cells were treated with different NPs for 3 to 6 h and MTT dye ( $0.5 \text{ mg ml}^{-1}$ ) was added after the treatment period. After incubation, the reaction mixture was carefully removed and formazan crystals were solubilized in 200  $\mu\text{l}$  dimethyl sulfoxide (DMSO). The interference of nanoparticles was obviated by centrifuging the plates, transferring the supernatant into a new plate and then measuring the absorbance at 550 nm in a SYNERGY-HT multiwell plate reader, Bio-Tek (USA) using KC4 software. The quantification of the cell

viability in terms of metabolically active cells was calculated using the formula below.

$$\% \text{Viability} = (\text{Mean Absorbance of Sample} / \text{Mean Absorbance of Control}) \times 100$$

***Escherichia coli* (*E. coli*) culture and exposure.** The *E. coli* (K12 sub-strain DH10B) was procured from MTCC, Chandigarh, India and cultured in 5 ml Luria Bertani (LB) broth at 37 °C for 12–16 h in an environmental shaker incubator at 180 rpm. One ml of overnight grown culture was re-inoculated in 100 ml LB broth and allowed to grow up to early log phase at an  $\text{OD}_{600}$  of 0.2–0.3 ( $1 \times 10^9 \text{ CFU ml}^{-1}$ ).  $5 \times 10^9$  cells (concentrated 5 ml culture) were treated with different NP concentrations ranging from 1–100  $\mu\text{g ml}^{-1}$  in PBS at 37 °C for 60 min.

**Bacterial cytotoxicity assay.** The toxicity assessment of the NP treated bacterial culture was carried out according to the protocol described by Jung *et al.*<sup>45</sup> Treated *E. coli* culture was washed twice with PBS and incubated with propidium iodide (PI) for 15 min at room temperature. The red fluorescence emitted from PI was collected using a  $650 \text{ nm} \pm 13 \text{ nm}$  band pass filter. The proportions of live and dead cell were determined and analyzed using BD FACSCanto II and FACSDiva™ software (Ver. 6.1.2).

### Thermal conductivity measurements

$\text{CuO}$  nanofluids were prepared by dispersing the as synthesized  $\text{CuO}$  nanoparticles in distilled water at a volume percentage of 0.1%. The thermal conductivity of the corresponding nanofluids was measured using hot disc thermal constant analyzer (model TPS-500).

## Results and discussion

### Microstructural features and phase formation

To evaluate the effect of pH on the morphological evolution of the  $\text{CuO}$  nanoparticles, we selectively prepared a series of samples using five different pH values of 7.25, 8.5, 10.0, 11.25 and 12.0 under parallel experimental conditions. The intermediate bluish precipitate, obtained immediately after the hydrolysis of the cupric salt, was characterized by XRD and SEM. The XRD patterns (Fig. 1) reveal a noteworthy sequence of events in terms of the component phases present in the intermediate. It was found that at lower pH values (7.25 and 8.5), the bluish precipitate consisted of mixed phase of materials, copper(II) hydroxy nitrate  $\{\text{Cu}_2(\text{OH})_3\text{NO}_3\}$  and copper(II) hydroxide  $\{\text{Cu}(\text{OH})_2\}$ , most of the peaks were characteristic of the hydroxy salt. The visible diffraction intensities corresponding to  $\text{Cu}_2(\text{OH})_3\text{NO}_3$  agree well with the peaks of monoclinic crystal structure of  $\text{Cu}_2(\text{OH})_3\text{NO}_3$  (JCPDS No.15-0014) with unit cell parameters  $a = 5.605 \text{ \AA}$ ,  $b = 6.087 \text{ \AA}$ ,  $c = 6.929 \text{ \AA}$  and  $\beta = 94.48^\circ$ . The diffraction intensities corresponding to  $\text{Cu}(\text{OH})_2$  were in agreement with the peaks of orthorhombic crystal structure (JCPDS No.035-505) and unit cell parameters  $a = 2.951 \text{ \AA}$ ,  $b = 10.592 \text{ \AA}$  and  $c = 5.273 \text{ \AA}$ . The intensity of the  $\text{Cu}_2(\text{OH})_3\text{NO}_3$  peaks reduce as we cross over from the pH 7.25 intermediate to



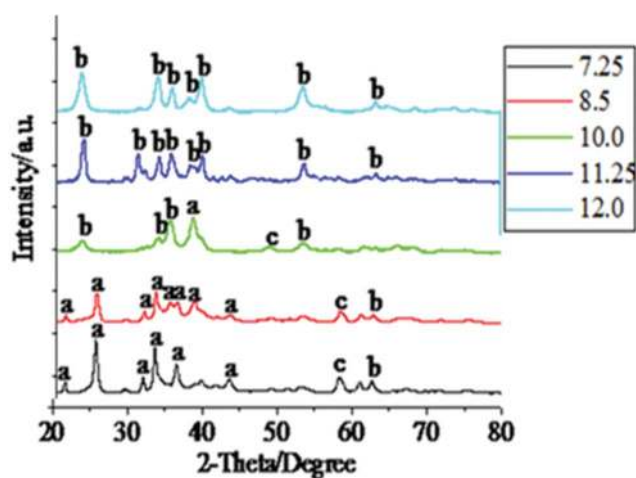


**Fig. 1** XRD patterns of the bluish products obtained by hydrolyzing  $\text{Cu}(\text{NO}_3)_2$  at different pH values. The pH values are shown in the inset. The patterns have been shifted for clarity.

the pH 8.5 intermediate, eventually becoming nonexistent in the higher pH region (10.0 onwards), where the peaks can all be identified with  $\text{Cu}(\text{OH})_2$  diffraction intensities. These observations tend to suggest that at lower pH the concentration of  $\text{OH}^-$  ions is not sufficient to replace all of the  $\text{NO}_3^-$  ions coordinated to the Copper atom. As a result, we get predominant formation of  $\text{Cu}_2(\text{OH})_3\text{NO}_3$  where Cu(II) atoms are coordinated to both  $\text{OH}^-$  and  $\text{NO}_3^-$  in a botallackite type crystal structure. The few peaks corresponding to  $\text{Cu}(\text{OH})_2$  present in the XRD patterns of the two low pH intermediates suggest the initial transformation to this species has begun. But on further increasing the pH (10.0 onwards) the obtained XRD patterns suggest the formation of only  $\text{Cu}(\text{OH})_2$  and no other species, indicating that at higher pH the concentration of  $\text{OH}^-$  is enough to convert  $\text{Cu}(\text{NO}_3)_2$  to  $\text{Cu}(\text{OH})_2$  completely. This is expected because previous works have shown that  $\text{Cu}_2(\text{OH})_3\text{NO}_3$  can be transformed to  $\text{Cu}(\text{OH})_2$  by treating it with a base.<sup>46</sup> Starting from the sample corresponding to pH 10.0, the peaks for  $\text{Cu}(\text{OH})_2$  become increasingly more intense and narrower with the increase in pH, suggesting an increase in crystallite size and better crystalline quality.

The SEM images of these intermediates (Fig. 2) projects the morphological evolution of these particles at varying pH values. When the pH is 7.25, the particles formed cannot be categorized under any particular shape. Round shaped, grain shaped and some wire like (with diameter in the range of 50–60 nm) structures are all visible (Fig. 2a). It is worth mentioning that the XRD of this sample showed the presence of a mixed phase of  $\text{Cu}(\text{OH})_2$  and  $\text{Cu}_2(\text{OH})_3\text{NO}_3$ , so the non-uniformity in the shapes can be attributed to the presence of two chemically distinguished components to some extent. The samples synthesized at pH 8.5 show more of a regular shape formation, with well defined seed-like particles (width of 120–150 nm, length varying between 350–400 nm) clearly observed (Fig. 2b). When the pH was raised to 10.0, the particles showed a tendency to grow longer vertically (600–700 nm) and in the process attained an ellipsoidal morphology (Fig. 2c). One interesting phenomena to note here is that at the higher pH region, the particles exist in bundles or, more precisely, an agglomerated form. The probable

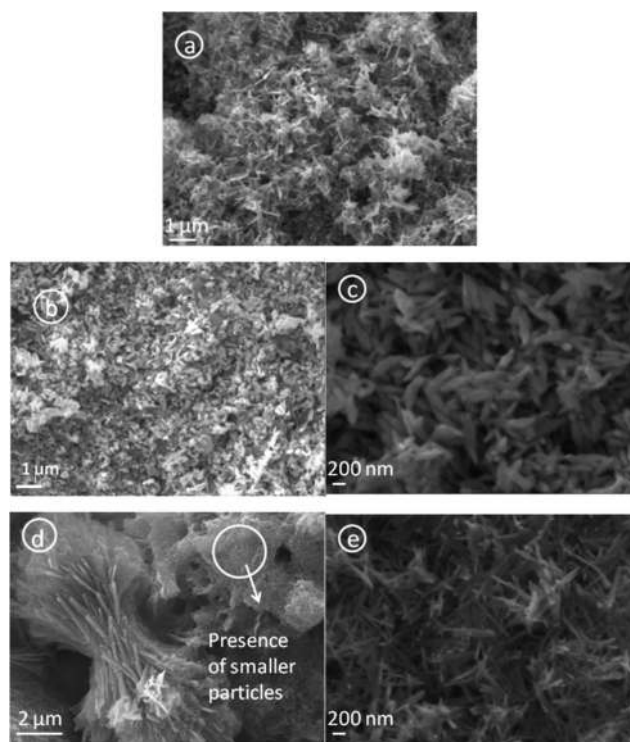


**Fig. 2** SEM micrographs of the bluish precipitates obtained after hydrolyzing  $\text{Cu}(\text{NO}_3)_2$  at different pH values. Micrographs correspond to a) pH 7.25, b) pH 8.5, c) pH 10.0, d) pH 11.25 and e) pH 12.0.

reason behind this agglomeration could well be the hydrogen bonding due to the high concentrations of  $\text{OH}^-$  species present in the particles. At pH 11.25, some plate shaped particles are observed (Fig. 2d) and these plates show a tendency to accumulate, producing flower-like topography of these accumulated nanostructures. There is also the simultaneous presence of a bunch of small particles (as shown in the encircled area in Fig. 2d) with an average width of about 50 nm and around 300 nm in length. This gives a possibility that the plates may have been formed by the smaller particles, as discussed later. At pH 12.0 we see the formation of rod shaped  $\text{Cu}(\text{OH})_2$  nanostructures about 20 nm in diameter and 400–500 nm in length (Fig. 2e) and following the trend, these particles too show preference for agglomeration, although to a much lower extent than what was observed at pH 11.25.

Fig. 3 shows XRD patterns of the CuO particles synthesized by annealing the blue precipitates at a temperature of 130 °C for 10 h at a stretch. The diffraction peaks for CuO were identified with respect to the JCPDS file No.45-0937; and crystal phase could be identified as monoclinic (unit cell parameters of  $a = 4.6853 \text{ \AA}$ ,  $b = 3.4257 \text{ \AA}$ ,  $c = 5.1303 \text{ \AA}$  and  $\beta = 99.549^\circ$ ). From the XRD patterns it is clearly observed that at the lower pH region (7.25 and 8.5), along with the peaks for CuO, few peaks of  $\text{Cu}_2(\text{OH})_3\text{NO}_3$  are also present. It presents the case that part of the  $\text{Cu}_2(\text{OH})_3\text{NO}_3$  has not been transformed to CuO on heating the sample. As we increase the pH from 7.25 to 8.5, the  $\text{Cu}_2(\text{OH})_3\text{NO}_3$  peaks diminish in intensity and finally disappear at pH 10.0 and above, the samples from pH 10.0 onwards were compositionally pure. On the other hand, the CuO peaks continued to grow in intensity and gradually became prominent

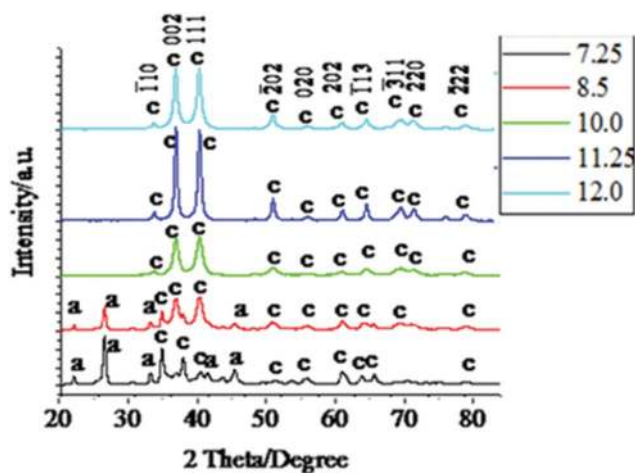


**Fig. 3** XRD patterns of the CuO nanoparticles synthesized by annealing the obtained precipitates of  $\text{Cu}(\text{OH})_2$  at a temperature of  $130\text{ }^\circ\text{C}$  for 10 h. Only the peaks corresponding to CuO are designated with corresponding hkl values in the plot. The corresponding pH values are shown in the inset. The patterns are shifted for clarity.

in appearance when the pH was increased. Also with the increase in pH, the CuO peaks became better defined, richer in intensity and sharper, suggesting an improvement in crystalline quality and crystallite size. Interestingly, in the lower pH region (7.25, 8.5 & 10.0) the 111 plane of the CuO nanocrystal is the most intense peak, but at pH 11.25 & 12.0 the 002 peak is the most intense. It indicates a change in preference for the crystal plane orientation as the pH increases. In addition to this, in the lower pH region the intermediate  $\{\text{Cu}(\text{OH})_2\}$  is relatively more unstable towards decomposition into CuO and the greenish shade of the intermediate indicates that some parts of the  $\text{Cu}(\text{OH})_2$  have already been transformed into black CuO. Presence of CuO peaks in the XRD pattern of these intermediates (Fig. 1) confirms it. In fact it was observed that, in the lower pH region, the entire precipitate would convert into CuO at room temperature itself within 15 h of the preparation of the  $\text{Cu}(\text{OH})_2$  precipitate. But to maintain uniformity in the process parameters we employed annealing induced decomposition of the intermediate for all the pH values.

The presence of  $\text{Cu}_2(\text{OH})_3\text{NO}_3$  in the intermediates at low pH values was further confirmed by the FT-IR spectra of the CuO samples (Fig. 4a–e). The peak centered at  $1048\text{ cm}^{-1}$  (present in the samples with the pH values 7.25, 8.5 and 10.0) arises due to  $\text{ONO}_2^-$  stretching.<sup>47</sup> Although no peak corresponding to the  $\text{Cu}_2(\text{OH})_3\text{NO}_3$  molecule for the pH 10.0 sample was observed in the XRD data, FT-IR reveals a very low intensity peak at  $1048\text{ cm}^{-1}$  indicating an extremely minute amount of  $\text{Cu}_2(\text{OH})_3\text{NO}_3$  still present in the sample. All the peaks present in the range of  $420\text{ cm}^{-1}$  to  $610\text{ cm}^{-1}$  and at  $1386\text{ cm}^{-1}$  correspond to the Cu–O stretching mode.<sup>46,48</sup> Curiously, these peaks show a prominent red shift as we move towards the samples synthesised at higher pH values, indicating a probable weakening or elongation of the Cu–O bonds.

Fig. 5 shows the SEM images of the as synthesized CuO nanoparticles acquired by thermal annealing of the bluish intermediates, synthesized at different pHs. Like their precursors, these particles also show a regular structural evolution with

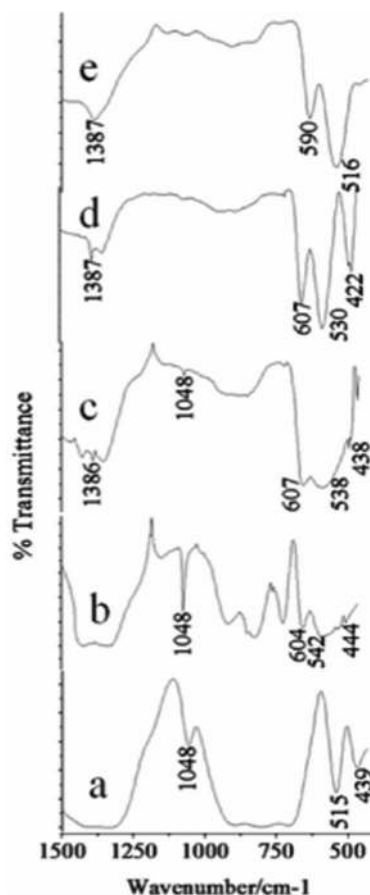


**Fig. 4** The FTIR spectra of the synthesized CuO nanoparticles synthesized at different pH values a) pH 7.25, b) pH 8.5, c) pH 10.0, d) pH 11.25 and e) pH 12.0.

the increase in pH. At the low pH 7.25, the image shows the predominant formation of grain like particles with no definite shape and size (Fig. 5a). At pH 8.5, the formation of seed-like particles was observed (with width of these particles in the range of 70–200 nm and the length 200–550 nm). Although most of the particles conformed to seed like shapes, as can be viewed in Fig. 5b,f, the HRTEM images of these particles reveal the simultaneous presence of some grain like particles (Fig. 6a) which were undetected in the SEM micrographs. The presence of these aberrations maybe attributed to the presence of  $\text{Cu}_2(\text{OH})_3\text{NO}_3$ , as detected by the XRD plots. Fig. 6b shows the HRTEM image of a single particle, clearly exposing the roughness of the surface and around the edges, suggesting that these seeds were formed by the accumulation of other smaller sized particles. The selected area electron diffraction (SAED) pattern shown in Fig. 6b (inset) also indicates the presence of mixed phases  $\{\text{CuO}$  and  $\text{Cu}_2(\text{OH})_3\text{NO}_3\}$  and due to the haziness in these patterns caused by the mixing of the phases all the lines could not be distinctively identified. Fig. 7 shows the difference between the SAED pattern of the mixed phase sample and that of a pure CuO sample. At pH 10.0, although the basic shape of these particles remains similar, the aspect ratio does not and the horizontal dimension shows a tendency to decrease (in the range of 90–175 nm) and the vertical dimension increases (in the range of 470–800 nm), thus gaining more of a ellipsoidal shape with



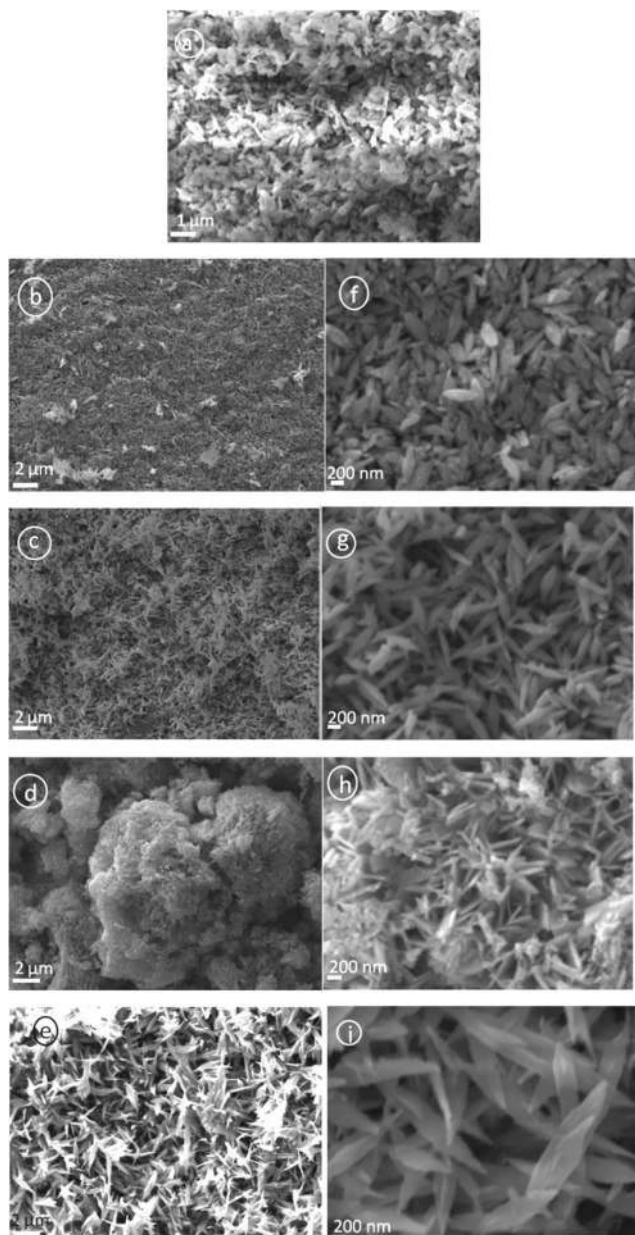


**Fig. 5** SEM images of the synthesized CuO nanoparticles; micrographs correspond to a) pH 7.25, b and f) pH 8.5, c and g) pH 10.0, d and h) pH 11.25, e and i) pH 12.0. Here too, except for the sample corresponding pH 7.25, micrographs of all the other samples have been produced for two different resolutions.

sharper edges. The sharpness of the terminal edges of these particles is quite prominently observed from the HRTEM image (Fig. 6c) and the uniformity in the shape is also quite evident. What is more exciting is the striking similarity in the shapes and the trend in shape evolution of the  $\text{Cu}(\text{OH})_2$  precursors and the CuO particles. The SAED pattern is shown in Fig. 6d (inset) and the polycrystalline nature of the sample was firmly established. The roughness of the surface is quite visible in the case of these particles too, as shown by the HRTEM image of an individual particle (Fig. 6d), giving away the fact that these particles were also formed by smaller subunits. As we go to pH 11.25, this trend of seed-like particles is broken and bundles of accumulated

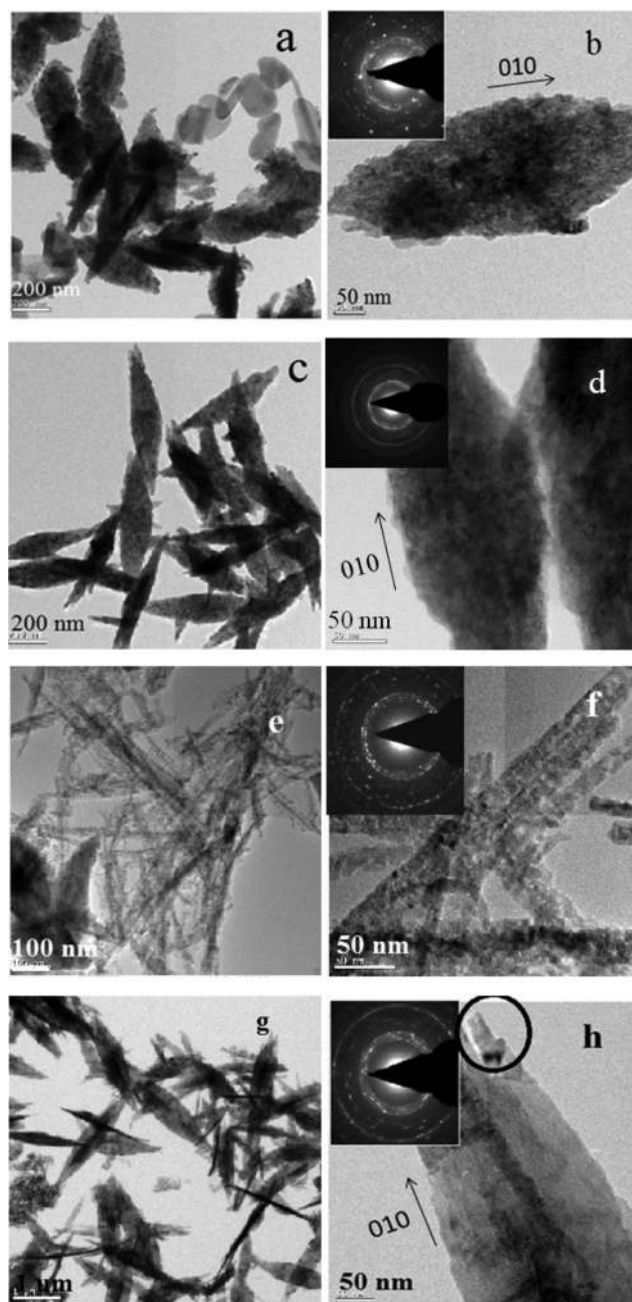


**Fig. 6** HRTEM micrographs of the synthesized CuO nanoparticles. (a–b) CuO synthesized at the pH 8.5. (c–d) CuO synthesized at the pH 10.0. (e–f) CuO synthesized at a pH 11.25. (g–h) CuO synthesized at a pH 12.0. SAED patterns are given in the inset.

particles with a flowery appearance were observed (Fig. 5d). A higher magnification SEM image (Fig. 5h) shows the presence of rod shaped particles with narrower diameters. The HRTEM image of these rods reveals the diameter to be in the range of 8–27 nm and the presence of smaller nanoparticles in a vertical accumulation is clearly visible (Fig. 6e), thus elucidating the fact that the rods themselves may actually be a result of the accumulation of much smaller particles. The SEM micrographs of the CuO samples corresponding to pH 12.0 shows the formation of leaf shaped particles with sharp terminal edges and semi-transparent visual aspect (Fig. 5e,i). These particles also

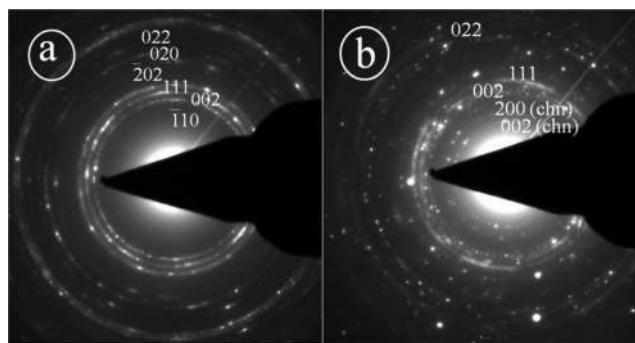


Fig. 7 SAED patterns of a) pure CuO phase b) mixed phase consisting of both CuO and  $\text{Cu}_2(\text{OH})_3\text{NO}_3$ , the latter is marked by chn.

possess large dimensions compared to the particles synthesized at other pHs, with the width in the middle 180–500 nm and the length in the range of 0.8–2.7  $\mu\text{m}$ . A detailed particle size distribution and aspect ratio distribution obtained from the HRTEM images for the CuO particles synthesized at the pH of 8.5, 10.0, 11.25 and 12.0, have been given in Fig. 8 in the form of histograms. From the particle size (particle width) distribution histogram (Fig. 8a) it can be concluded that both the seed-like and the ellipsoidal particles, synthesized at pH 8.5 and 10.0 respectively, are dominated by particles of widths within 100–150 nm, but the aspect ratio (Fig. 8b) of the former (mostly within 1.5–3.5) is much less compared to the ellipsoidal particles (3–6). The width of the leaf shaped particles are stretched over a wide range, Fig. 8a reveals that the particles within 400–450 nm are dominant. However the aspect ratios (Fig. 8b) of these particles are mostly within 3–7 which is very similar to the ellipsoidal particles. The nanorods have their diameter mostly around 20 nm and the aspect ratio varies from 8–27.

The HRTEM image of an individual leaf shows two rod shaped structures protruding from its terminal area, (Fig. 6h; encircled area), giving out the indication that these thin leaves might well have been formed from the special reorientation of the rod shaped particles. Both the samples (pH 11.25 & 12.0) are polycrystalline, as was evident from their respective SAED (Fig. 6e,g). Combined with the SAED pattern (which has rings associated with the 001 zone axis) and the HRTEM images, 010 has been determined as the growth direction of the nanoparticles.

This long axis direction is vertical to the lattice interplanar spacings and 001 and 100 are determined to be the enclosing top and side planes, respectively. Due to the difference in aggregation potential and rate and the fact that the number of primary nanocrystals assembled in the three directions are significantly different, for CuO, 001 is thermodynamically the most stable surface plane while 010 is the least. So the particles tend to aggregate more towards the 010 direction and the least towards the 001 direction.

### Mechanism for the evolution of different nanostructural patterns

The growth mechanism of these CuO nanoparticles and its mercurial shape evolution can be explained by taking the growth pattern and chemistry of their corresponding  $\text{Cu}(\text{OH})_2$  precursor formation into account. In aqueous solution,  $\text{Cu}(\text{NO}_3)_2 \cdot 3\text{H}_2\text{O}$  dissociates into  $[\text{Cu}(\text{H}_2\text{O})_6]^{2+}$  ions (responsible for the sky blue coloring) and  $\text{NO}_3^-$  anions. In the  $[\text{Cu}(\text{H}_2\text{O})_6]^{2+}$  structure, six water molecules completely surround each  $\text{Cu}^{2+}$  ion, shielding it. Due to the solvating action when copper salt is dissolved in water, four water molecules surround the  $\text{Cu}^{2+}$  to form a square structure  $\text{Cu}(\text{OH})_4^{2-}$ , and the other two water molecules locate at its axis. According to the anionic coordination polyhedra theoretical model,<sup>46</sup> cations exist in the form of complexes whose ligands are  $\text{OH}^-$  ions in an aqueous solution; a complex with coordination numbers equal to that of the crystal formed is called a growth unit. Moreover, the formation of growth units and the incorporation of the growth units into the crystal nucleus are induced by a dehydration reaction. Accordingly, the growth units for  $\text{Cu}(\text{OH})_2$  nanocrystals are considered  $\text{Cu}(\text{OH})_6^{4-}$ , a coordinating octahedron in the NaOH solution. In this case, four  $\text{OH}^-$  ions are arranged on a planar square, and the other two  $\text{OH}^-$  ions are located on a perpendicular axis. The binding energies of the two  $\text{OH}^-$  ions located on the octahedron axis are lower than those of  $\text{OH}^-$  located on the plane.<sup>49</sup> This means that the two  $\text{OH}^-$  ions located at the axis are easily replaced and dehydrated to form CuO nanocrystallites, so that the growth rate along the axes is higher than in the plane. The growth mechanism and formation of different shapes of CuO nanocrystals (*e.g.* nanorods, nanoseeds, *etc.*) can be explained with this difference in growth rates along various directions. At high temperatures (130  $^\circ\text{C}$  in this synthesis) the hydrogen bonds which interconnects the  $\text{Cu}(\text{OH})_2$  particles are mostly destroyed,

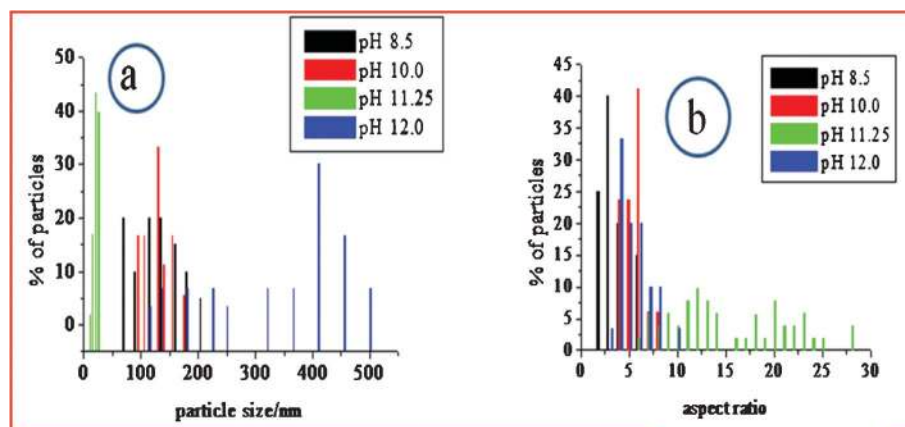
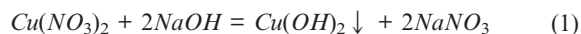


Fig. 8 Histograms derived from the HRTEM images showing a) particle size distribution, b) aspect ratio distribution.



thus the formation of randomly shaped particles is prohibited and a particular shape is favored. Also, because  $\text{Cu}(\text{OH})_2$  is a layered material and the growth rate is anisotropic,  $\text{Cu}(\text{OH})_2$  adopts a morphology with unequal dimension rather than with spherical appearance and prefers a morphology with one dimension longer than the others. The formation mechanism of the  $\text{CuO}$  nanostructures is easy to understand. During the heating process, the  $\text{Cu}(\text{OH})_2$  nanoparticles lose  $\text{H}_2\text{O}$  molecules and transform into  $\text{CuO}$  while its morphology still remains. This is why the morphology of the  $\text{CuO}$  nanoparticles closely resemble the  $\text{Cu}(\text{OH})_2$  precursors. The formation of different nanostructures like seeds, rods or ellipsoids can be strongly related to the morphology and dimensionality of the primary subunits. The chemical reaction that occurs during the process is illustrated below:

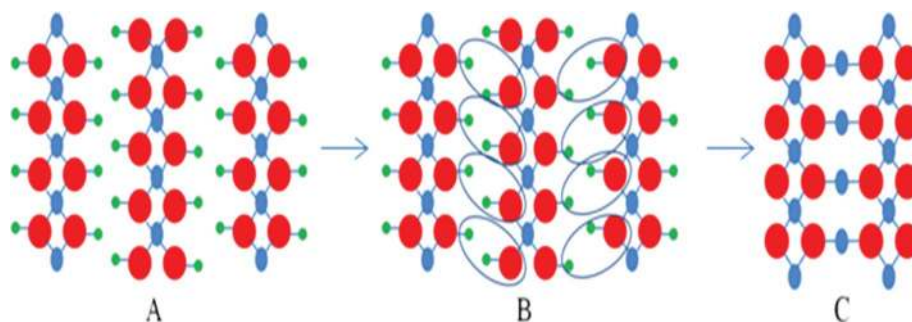


The loss of water is performed by an oxolation mechanism, which involves a dehydration process and the formation of O–Cu–O bridges. A schematic illustration of this dehydration process has been depicted in Scheme 1.

From a kinetic point of view, step 2 of the above process is the rate determining step of the reaction because the approach of two negatively charged hydroxyl ions to a di-acidic base is kinetically unfavorable and as a result makes the process slower. The rate of formation of  $\text{Cu}(\text{OH})_4^{2-}$  and the momentary concentration of this species relative to the hydroxyl ions have utmost bearing on the eventual formation of  $\text{CuO}$  via the dehydration of  $\text{Cu}(\text{OH})_2$ . The excess concentration of alkali aid the reaction to move more towards the right side of equilibrium, resulting in the fast generation of  $\text{Cu}(\text{OH})_4^{2-}$  which can quickly convert into  $\text{Cu}(\text{OH})_2$  forming a regular 1-D chain whereas the slower generation of  $\text{Cu}(\text{OH})_4^{2-}$  lets more hydroxyl ions interact during the formation process, allowing them to be involved in the chain forming process and thus the shape of the resultant particle becomes ill defined. At a more primitive level, the ongoing crystallographic transformation is also noteworthy. A

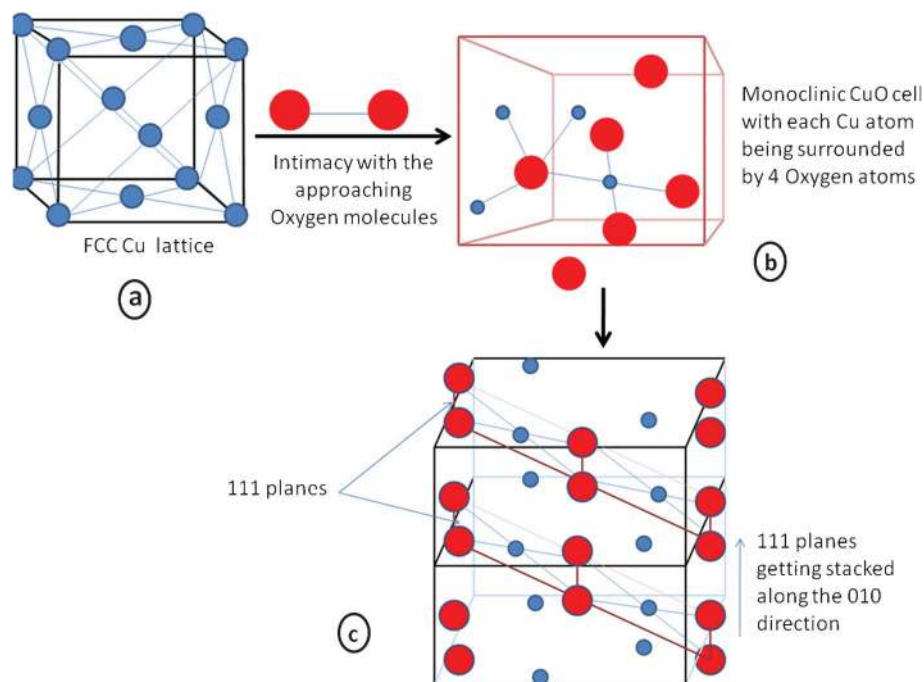
schematic diagram of this metamorphosis is presented in Scheme 2 to illustrate this process. Here the face centered cubic lattice of Cu (Scheme 2a), when intimated with oxygen molecules produces molecules of  $\text{CuO}$ . During the formation of the  $\text{CuO}$  lattice each Cu atom gets surrounded by four oxygen atoms, giving it a coordination number of 4 (Scheme 2b) and forming dominant 111 planes, which in turn get aligned and stacked along the growth direction of 010 (Scheme 2c). But these oxygen atoms, when entering the lattice of Cu the FCC unit cell of Cu no longer exist for obvious reasons and through various atom rearrangements and lattice/unit cell reconstruction, the monoclinic unit cell of  $\text{CuO}$  is generated. The high symmetry FCC lattice of Cu and the low symmetry monoclinic unit cell of  $\text{CuO}$  have considerable energy differences, but the structure is stabilized due to the highly stable  $\text{Cu}^{2+}$  valence state. Although the schematic may not necessarily be an exact picture of the mechanistic details, it presents a simple depiction of the transformation that takes place at the atomic level.

Due to the presence of mixed phases at a lower pH (7.25), no particular shape could take precedence but the presence of some nano wires could be seen (Fig. 2a). But at a higher pH (8.5), a more definite particle shape is observed and the particles formed are seed-like or semicircular, indicating that the anisotropic growth of the  $\text{Cu}(\text{OH})_2$  nanoparticles, which is subsequently dehydrated to produce  $\text{CuO}$  with the morphology of its precursor  $\text{Cu}(\text{OH})_2$  (Fig. 2b,f). These particles are the result of aggregation of smaller subunits, as indicated by the HRTEM image (Fig. 6b). The HRTEM image (Fig. 9a) exhibits regular spacing of the clear lattice plane of 0.23 nm which corresponds well to the (111) lattice plane of the monoclinic phase  $\text{CuO}$ . At pH 10.0, the formation of flake or ellipsoidal shaped particles is a consequence of further anisotropic growth of the  $\text{Cu}(\text{OH})_2$  nanoparticles bolstered by the more availability of the  $\text{OH}^-$  ions which help in bridging smaller subunits in a particular direction. When the pH was increased further, the presence of excess  $\text{OH}^-$  ions force the particles to agglomerate via hydrogen bonding (in the region around pH 11.25), forming flower-like assemblage of  $\text{Cu}(\text{OH})_2$  plates. The presence of seed-like particles along with the plates (Fig. 2h) exposes the fact that smaller seeds are behind the formation of these plates as units. Annealing causes these plates to break into nanorods of  $\text{CuO}$  which themselves are composed of smaller subunits, in fact the entire structure is constituted of nanocrystallites of the same phase ( $\text{CuO}$  monoclinic) with different orientations of varied interplanar spacings. As an illustrative example, Fig. 9b elucidates the presence of two



**Scheme 1**  $\text{Cu}(\text{OH})_2 \rightarrow \text{CuO}$  transformation process; green balls represent hydrogen atoms, blue balls represent copper atoms and red balls represent oxygen atoms. A)  $\text{Cu}(\text{OH})_2$ , B) loss of water molecules, C)  $\text{CuO}$  (oxolation process).





**Scheme 2** Schematic representation of the formation of CuO at a molecular level from a crystallographic perspective. The blue balls represent Cu atoms and the red balls represent oxygen atoms. a) the FCC lattice of Cu ; b) the monoclinic cell of CuO ; c) two unit cells joint by a common face, showing the stacking of the 111 planes.

prominent nanocrystals (marked as A and B) with the corresponding plane spacing 0.25 nm and 0.23 nm of hkl (002) and (111) of the monoclinic CuO crystal structure, respectively. These nanocrystals make an orientation angle of approximately  $50^\circ$  between them. Moreover a thin grain boundary with a

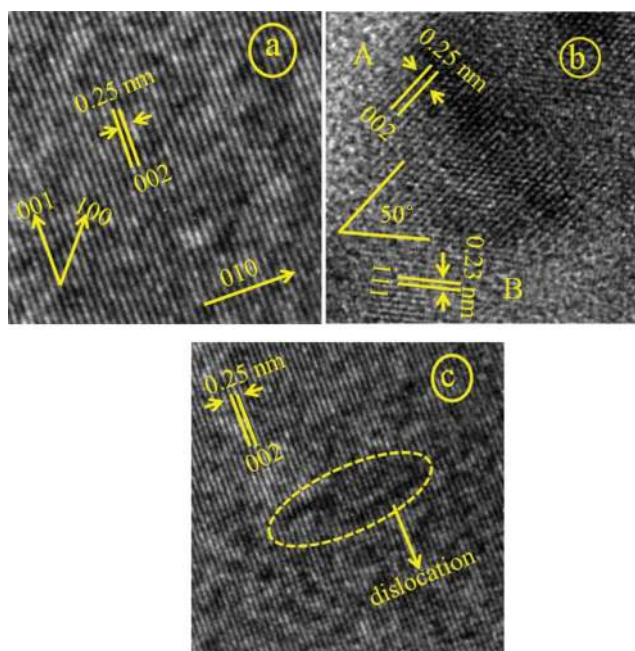


**Fig. 9** HRTEM image showing the lattice scaling of the CuO samples corresponding to a) pH 8.5 b) pH 11.25 c) pH 12.0; the growth direction is shown in image a as 010. 001 and 100 are the two other perpendicular directions where the growth is not favoured.

diffused contrast can also be seen between the crystals A and B. In general the grain boundaries are constituted with a major fraction of defects leading to an amorphous like structure which in turn reflects a featureless (diffused) contrast in high resolution images which is expected, keeping in mind the structural transformation that is on the way. This is also consistent with the XRD result which show that the relative intensity of the (002) and (111) undergoes a reversal in this pH region. At an increased pH (12.0) a critical point is reached where the plates of  $\text{Cu}(\text{OH})_2$  dissociate into nanorods of  $\text{Cu}(\text{OH})_2$  (Fig. 2e,i). So at around pH 11.25, a fascinating structural transformation begins which eventually leads to the formation of nanorods at around pH 12.0. On annealing, these nanorods produce the leaf shaped CuO particles upon stacking with each other while dehydration. The presence of the rods in the HRTEM image of the CuO particles corresponding to pH 12.0 (Fig. 6h; encircled area) proves that the leaves are resultant structures of the special orientation of the nanorods. An HRTEM image of the sample (Fig. 9c) provides the interplanar spacing of 0.25 nm or the equivalent (002) plane of the monoclinic CuO crystal system as the plane along the growth direction. The driving force that is involved in the accumulation of the smaller subunits or nanocrystals into bigger nanoparticles deserves a special mention. We obtained our CuO nanoarchitectures without using surfactants, ligands, polymers or templates. So we can convincingly leave out a variety of driving forces such as ligand exchange or the removal of stabilizing agents from the nanocrystal surfaces. Aggregation through dipolar interactions can also be ruled out with regard to the crystal structure of monoclinic CuO. Although nonprotected and weakly protected nanocrystals were thought to undergo entropy driven random assembly, it was recently affirmed by Lee *et al.* that “oriented attachment” was an effective and

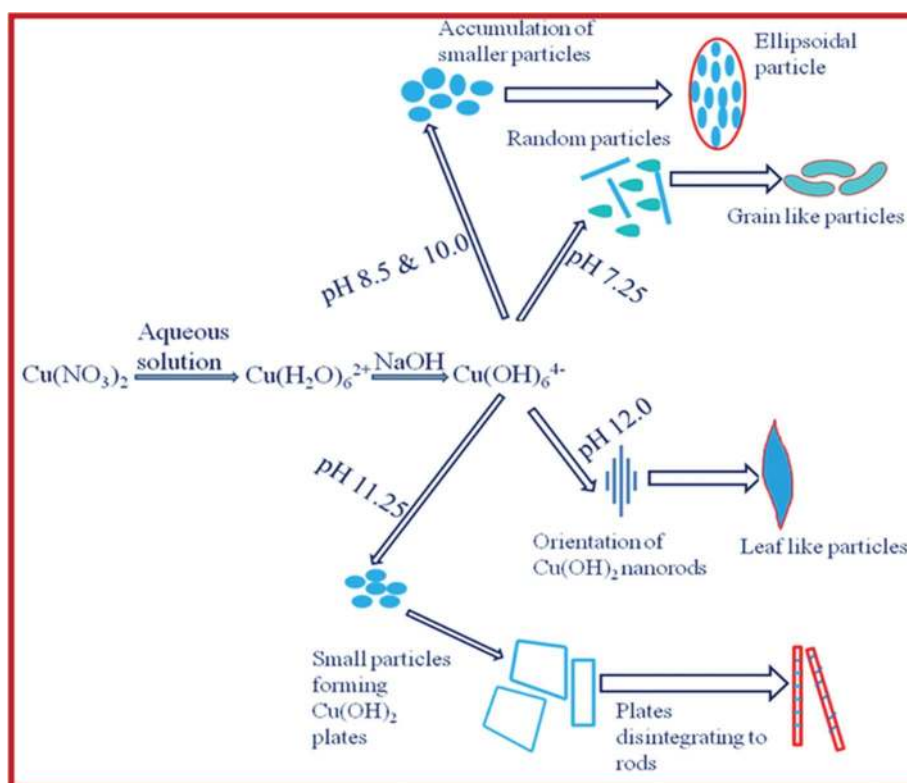
general mechanism in the formation of anisotropic nanoparticles.<sup>50</sup> The mechanisms associated with their work were i) the rotation of misaligned adjacent nanoparticles to share an identical crystallographic orientation and thus form configurations of minimum energy and ii) by collisions of aligned nanoparticles in suspensions. Since growth by oriented collision induced attachment is statistical, and generally leads to the formation of structures with random morphologies, the former mechanism seems to be the better suited to explain the aggregation of CuO nanocrystals into the 3D shapes we have obtained. The presence of dislocations in the bonding interfaces (Fig. 9c) clearly proves that the leaves of CuO were formed by the oriented attachment mechanism, as the formation of dislocations in the bonding interfaces is a direct consequence of the oriented attachment growth. An overall skeleton of the reaction mechanism is presented in the form of a schematic diagram in Scheme 3.

### Characteristic emission states and energy band gap

The CuO band gap and its general optical properties have been studied by optical absorption or UV-Vis studies with results showing the variation in its optical band gap ( $E_g$ ) with the size variation at the nanoscale. Luminescence techniques, which are important tools for investigating electronic transitions in semiconductors, including band edge or near band edge emissions (NBE) transitions, have seldom been used in case of CuO. The reason behind lack of luminescence data for CuO is largely due to the low emission efficiency of this material. Here in this work we report CuO particles showing photoluminescent

properties and the intensity of these luminescence bands could be dictated by varying their shapes which we achieved by altering the process conditions.

Here both the UV-Vis spectroscopy and photoluminescence probe were performed by taking the aqueous dispersion of the as synthesized CuO nanoparticles. Fig. 10 shows the room temperature absorption and photoluminescence spectrum of the samples. The UV-Vis pattern (Fig. 10a) displays a broad absorption peak in the wavelength range 270–360 nm and the curve within the region 290–340 nm is almost horizontal. Subsequently the photoluminescence spectroscopy was performed at an excitation wavelength of 370 nm. Interestingly the luminescence spectra of the rod shaped particles vary quite a lot from the corresponding spectra of seed-like, ellipsoidal and leaf shaped particles (Fig. 10b). The later three have identical looking spectra in terms of the positioning of the peaks with each having only one peak in the red region of the visible band at 667 nm. The peak in the red band region can be attributed to the NBE emission of the as synthesized CuO particles. The corresponding energy of this emission is about 1.86 eV which is close to the higher limit of the CuO optical band gap (1.2–1.8 eV). The seed-like particles show the most intense peak amongst the three followed by the ellipsoidal particles and the leaf-shaped particles have the lowest intense peak, revealing a trend that is consistent with the dimensions of the respective particles. The NBE peak for the rod-like particles is suppressed, which is quite curious because the NBE emissions in semiconductors have an inverse dependence on the particle diameter. So the CuO nanorods with the lowest particle diameter are supposed to have the most intense NBE peak.



**Scheme 3** Pictorial representation of the formation of various shapes of CuO under different synthesis conditions.

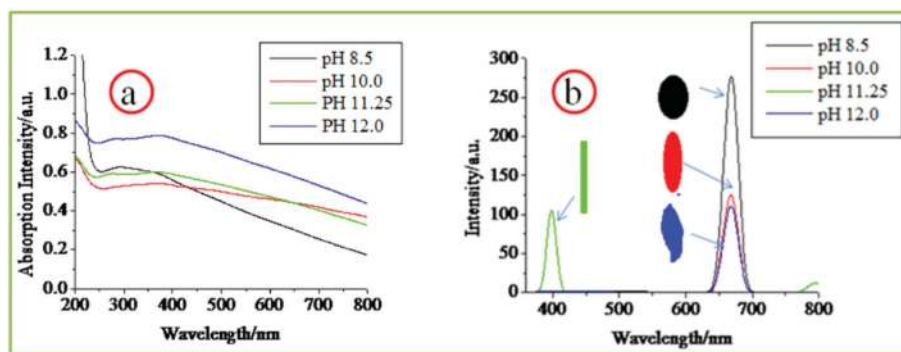


**Fig. 10** Room temperature optical properties of different CuO nanostructures revealed by a) UV-Vis absorption spectroscopy and b) photoluminescence spectroscopy.

The reason behind this anomalous behavior requires further experimental investigation. The UV-violet emission (398 nm), which is observed exclusively for the rod shaped particles may be due to phonons engendered by the trapped charge carriers generated by crystal lattice defects induced by strain or dangling bonds at the surface induced crystal lattice defects.

#### Evaluation of the toxic response of the CuO nanoparticles

In the present study, the toxicity of CuO nanoparticles were assessed in mammalian (Chinese hamster ovary; CHO) and bacterial (*Escherichia coli*; *E. coli*) cells. CHO cells were used since they do not possess metabolic capability and are recommended by the OECD (Organization for economic co-operation and development) for toxicity assessment of the parent compound. *E. coli*, which on the other hand, is a ubiquitous organism and plays an important role in element cycling, degradation of pollutants and other chemicals, was used as a model organism to detect any adverse effects of NPs on the environment. A recent study has shown that it can be used for the eco-toxicity risk assessment of nanoparticles.<sup>51</sup>

The mean hydrodynamic diameter of CuO NPs corresponding to different synthesis pH's in F12 media as measured by dynamic light scattering (DLS) were 238 nm (pH 8.5), 287 nm (pH 10.0), 245 nm (pH 11.25) and 489 nm (pH 12.0) while the zeta potential was -12.1, -10.2, -12.3 and -11.3 mV, respectively (Table 1). The average size of the particles was also found to be proportionate to the width and length of the particles. The size distribution of the particles is shown in Fig. 11. The hydrodynamic diameter and the overall size distribution of the particles was higher than their corresponding TEM size as it includes a few solvent layers,<sup>51</sup> but the presence of several columns indicates that the particles were well dispersed in the medium which is critical for our experiment.

**Table 1** Hydrodynamic diameter and the corresponding zeta potentials for the four different CuO nanoparticles synthesized under varying pH

| Nanoparticles      | Hydrodynamic diameter (nm) | Zeta potential (mV) |
|--------------------|----------------------------|---------------------|
| CuO NPs (pH 8.5)   | 238.8                      | -12.1               |
| CuO NPs (pH 10.0)  | 287.2                      | -10.2               |
| CuO NPs (pH 11.25) | 245                        | -12.3               |
| CuO NPs (pH 12.0)  | 489                        | -11.3               |

**Mitochondrial activity.** The MTT assay is a well known method to assess the toxicity of the compound on cellular system under *in vitro* condition. In this assay, yellow tetrazolium MTT dye is reduced by succinate dehydrogenase enzymes produced by mitochondria of the metabolically active cells and form formazan crystals. The spectrophotometric quantification of the solubilized formazan corresponds to the viability of the cells. Our data demonstrates a statistically significant ( $p < 0.05$ ) cytotoxic effect of CuO NPs in CHO cells at concentrations 50 and 100  $\mu\text{g ml}^{-1}$  after 3 h exposure. MTT results demonstrated that mitochondrial succinate dehydrogenase activity was reduced to 79% and 38% (relative to 100% of control; pH 8.4) 94%, 45% (pH 10), 79%, 57% (pH 11.25) and 85%, 69% (pH 12) respectively at only the two higher concentrations (50 and 100  $\mu\text{g ml}^{-1}$ ) after 3 h exposure (Fig. 12). The figure also clearly indicates that for 3 h incubation time substantial cytotoxicity is observed only beyond the 30  $\mu\text{g ml}^{-1}$  concentrations. However, at 6 h a significant cytotoxicity of the NPs was observed at 10, 20, 30, 50 and 100  $\mu\text{g ml}^{-1}$  concentrations (Fig. 12). Our data demonstrated that a variation in size and length is directly correlated with cytotoxicity. Previously, Karlsson *et al.*<sup>52</sup> had demonstrated the cytotoxicity of 20–40 nm size CuO NPs in lung cell line (A549) at 80  $\mu\text{g ml}^{-1}$  concentration after 18 h exposure. However, the data from the present study exhibited a higher cytotoxicity of the NPs at lower concentrations and time of exposure. CuO NPs synthesized at pH 12 exhibited maximum toxicity after the incubation time of 6 h, although after 3 h incubation time it seems to be comparatively less toxic, which may be due to the greater penetration and retention of the particles in the cell, as it has least vertical width (20 nm) or least thickness. The percent viability of the cells at different concentrations and time points are mentioned in Table 2.

**Bacterial cytotoxicity assay.** Our data demonstrates a statistically significant ( $p < 0.05$ ) cytotoxicity of CuO NPs at concentrations 10, 50 and 100  $\mu\text{g ml}^{-1}$  after 1 h exposure (Fig. 13). The maximum toxicity was observed with the leaf shaped CuO particles formed at pH 12.0 which consistent with the MTT results. One very interesting observation here is that although the bacterial cytotoxicity assay increases with increasing concentration, the increase is not linearly related with the concentration. At a lower concentration region the cytotoxicity increases rapidly with increasing concentration,



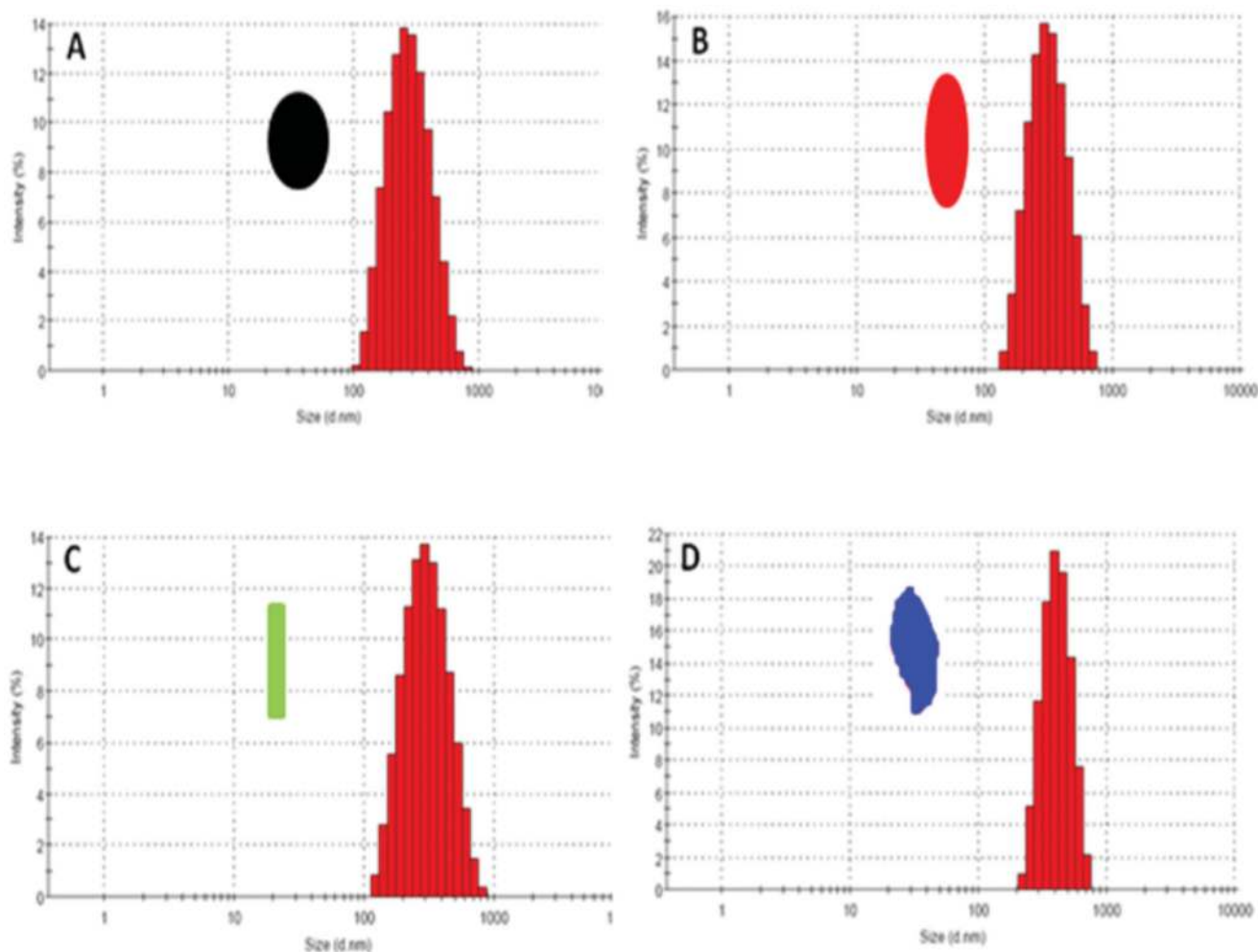


**Fig. 11** Intensity based particle size distribution of the different CuO NPs corresponding to different synthetic pH obtained from dynamic light scattering method. A) pH 8.5 (seed-like), B) pH 10.0 (ellipsoidal), C) pH 11.25 (rods), D) pH 12.0 (leaf-like).

but beyond that region the rate of increase is slow indicating the possibility of an optimum concentration for the maximum cytotoxicity.

The reason for the cytotoxicity induced by the CuO nanoparticles or other nanoparticles has been a much debated issue for scientists for some time. The two commonly accepted paradigms for toxicity are i) the generation of reactive oxygen species (ROS) and ii) induction of oxidative stress in the cells. As the particle diameter approaches the nanoscale dimension, the surface area of the particles increases significantly leading to the availability of chemically reactive functional groups on the surface that could play a role in the adverse biological effects. For instance, a change in the material properties to create discontinuous crystal planes or enhance of electron storage can contribute to ROS generation. Alternatively, the increased surface reactivity could lead to protein denaturation, membrane damage, DNA cleavage, immune reactivity, and inflammation. Ultimately the effect of the small particle size combined with the particle number and surface area determine the actual dose of exposure. Toxic oxidative stress can perturb mitochondrial function in a number of ways, including disruption of electron flow in the inner membrane, dissipation of the mitochondrial

membrane potential ( $\Delta\psi_m$ ), mitochondrial  $\text{Ca}^{2+}$  uptake, and large-scale opening of the PTP.<sup>53</sup>

It may look anomalous that the CuO particles synthesized at pH 12.0, despite having the largest particle size (confirmed from both HRTEM and DLS measurements) elicit the maximum toxicity. Although the decreasing particle size generally produces more toxic effects due to the increment in surface to volume ratio, here the leaf shaped particles, because of their peculiar disposal of surface features, are able to induce more surface related phenomena and are more suited to generate ROS on their surfaces. Earlier reports have indicated that bio-toxicity generated by CuO nanoparticles may be due to the release of soluble  $\text{Cu}^{2+}$  ions, which may enter the cells causing enhanced cytotoxicity.<sup>12</sup> From the FTIR spectra of the CuO nanoparticles (Fig. 4) it was observed that the bonds corresponding to Cu–O stretching went for a slight lowering in energy for the pH 12.0 sample when compared to the other samples ( $607\text{ cm}^{-1} \rightarrow 590\text{ cm}^{-1}$ ;  $530\text{ cm}^{-1} \rightarrow 516\text{ cm}^{-1}$ ), indicating a slightly increased Cu–O bond length for the leaf shaped particles, rendering it more susceptible to dissociation and subsequently yielding  $\text{Cu}^{2+}$  ions, eventually leading to increased cytotoxicity. Any of the reasons discussed above, or the synergistic effect of all of them

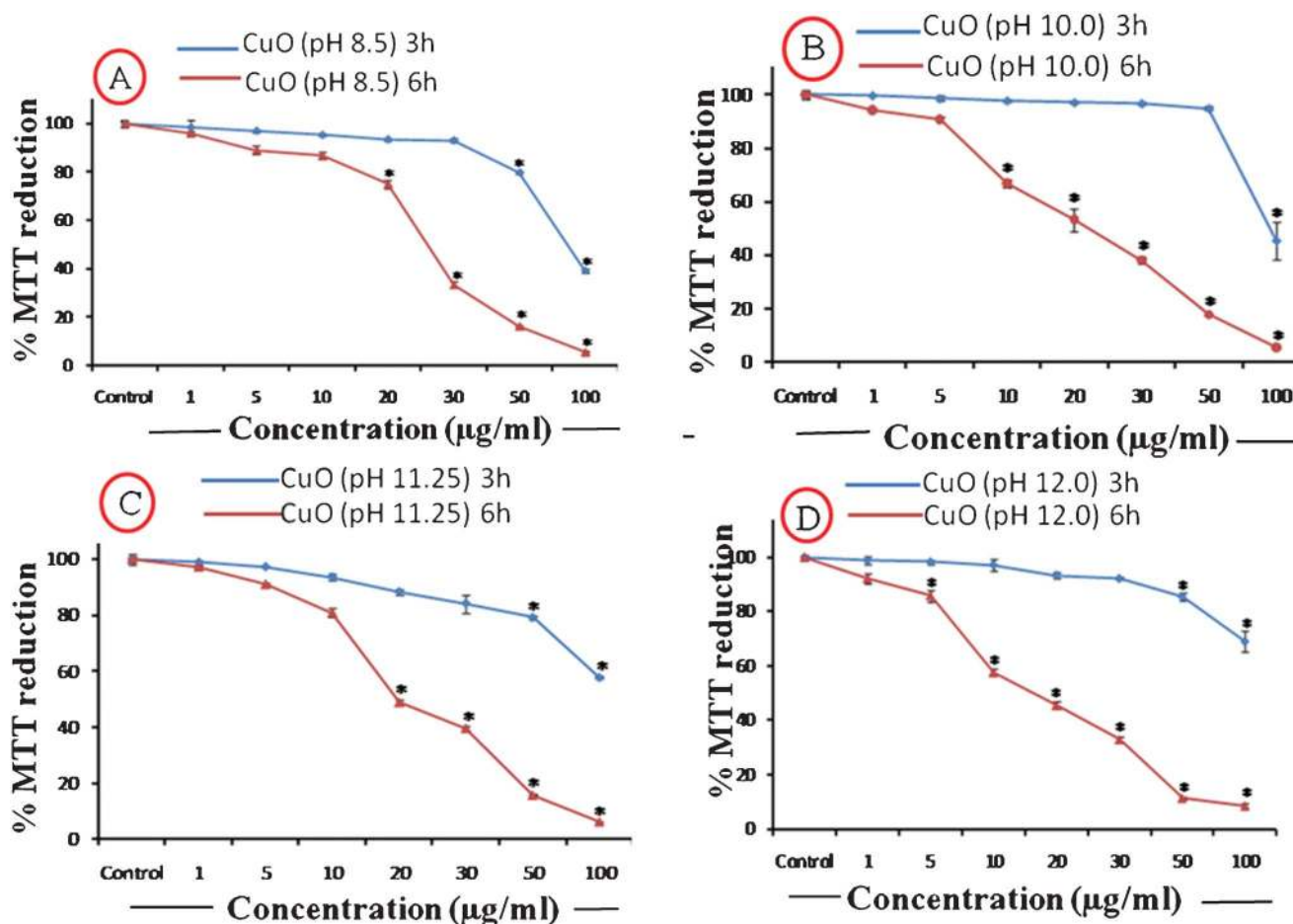


Fig. 12 %MTT reduction caused by the Different CuO NPs applied at a concentration range of 1–100  $\mu\text{g ml}^{-1}$  for two time durations of 3 h and 6 h.

can lead to the enhanced cytotoxicity of the leaf shaped particles synthesized at pH 12.0.

#### Evaluation of thermal conductivity of nanofluids prepared from the as synthesized CuO nanoparticles

Fig. 14 shows the percentage thermal conductivity (TC) increment for different temperatures within a temperature region of 20–80 °C for the nanofluids prepared by dispersing 0.1% CuO nanoparticles (in terms of volume) in distilled water. It evidently shows the efficiency of our synthesized CuO nanoparticles in enhancing the thermal conductivity. Although

no real trend in terms of the relation between temperature and TC increment could be established from the obtained data, we were able to observe particulars with respect to the shape of the three CuO nanoparticles corresponding to pH 8.5, 10.0 and 11.25 (sample A, B, C respectively). It should be noted that the particles corresponding to synthetic pH 12.0 were excluded from the measurement because it was observed that their dispersion in water was not stable or uniform for a sufficiently long period of time to enable us to carry out the measurement. We did not add any external stabilizing agent in order to avoid the complications that would arise during the interpretation of the result and also to avoid its effect on the TC itself. The

**Table 2** Percent cell viability of nanoparticles treated CHO cells at different concentrations and incubation time. The data are expressed as means  $\pm$  SEM from three independent experiments. The values in bold are significant ( $p < 0.05$ ) when compared to control

| CuO NP concentration      | Condition    |              |                |              |              |              |                |              |
|---------------------------|--------------|--------------|----------------|--------------|--------------|--------------|----------------|--------------|
|                           | pH 8.4       |              | pH 10          |              | pH 11.25     |              | pH 12          |              |
|                           | 3 h          | 6 h          | 3 h            | 6 h          | 3 h          | 6 h          | 3 h            | 6 h          |
| 1 $\mu\text{g ml}^{-1}$   | 98 $\pm$ 5.4 | 96 $\pm$ 1.1 | 99 $\pm$ 0.2   | 94 $\pm$ 2.3 | 98 $\pm$ 1.1 | 97 $\pm$ 1.4 | 98.9 $\pm$ 2.6 | 92 $\pm$ 2.9 |
| 5 $\mu\text{g ml}^{-1}$   | 96 $\pm$ 0.8 | 89 $\pm$ 3   | 98.6 $\pm$ 1.8 | 90 $\pm$ 0.3 | 97 $\pm$ 0.1 | 91 $\pm$ 0.8 | 98.3 $\pm$ 1.1 | 85 $\pm$ 3.6 |
| 10 $\mu\text{g ml}^{-1}$  | 95 $\pm$ 0.7 | 86 $\pm$ 2.5 | 97.8 $\pm$ 1   | 66 $\pm$ 2   | 93 $\pm$ 1.7 | 80 $\pm$ 1   | 97 $\pm$ 3.6   | 57 $\pm$ 2.2 |
| 20 $\mu\text{g ml}^{-1}$  | 93 $\pm$ 1   | 75 $\pm$ 3.1 | 97.1 $\pm$ 1   | 53 $\pm$ 2.6 | 88 $\pm$ 1.7 | 48 $\pm$ 3   | 93.4 $\pm$ 1.7 | 45 $\pm$ 2.8 |
| 30 $\mu\text{g ml}^{-1}$  | 92 $\pm$ 1.1 | 33 $\pm$ 2.1 | 96 $\pm$ 0.6   | 38 $\pm$ 4   | 84 $\pm$ 5.8 | 39 $\pm$ 1.5 | 92 $\pm$ 0.7   | 32 $\pm$ 2.1 |
| 50 $\mu\text{g ml}^{-1}$  | 79 $\pm$ 1   | 16 $\pm$ 0.9 | 94 $\pm$ 1.5   | 17 $\pm$ 0.7 | 79 $\pm$ 1.4 | 15 $\pm$ 0.4 | 85 $\pm$ 1.3   | 11 $\pm$ 0.7 |
| 100 $\mu\text{g ml}^{-1}$ | 38 $\pm$ 1.5 | 6 $\pm$ 0.8  | 45 $\pm$ 0.6   | 6 $\pm$ 0.6  | 57 $\pm$ 0.7 | 6 $\pm$ 0.2  | 69 $\pm$ 3.7   | 8 $\pm$ 1.2  |

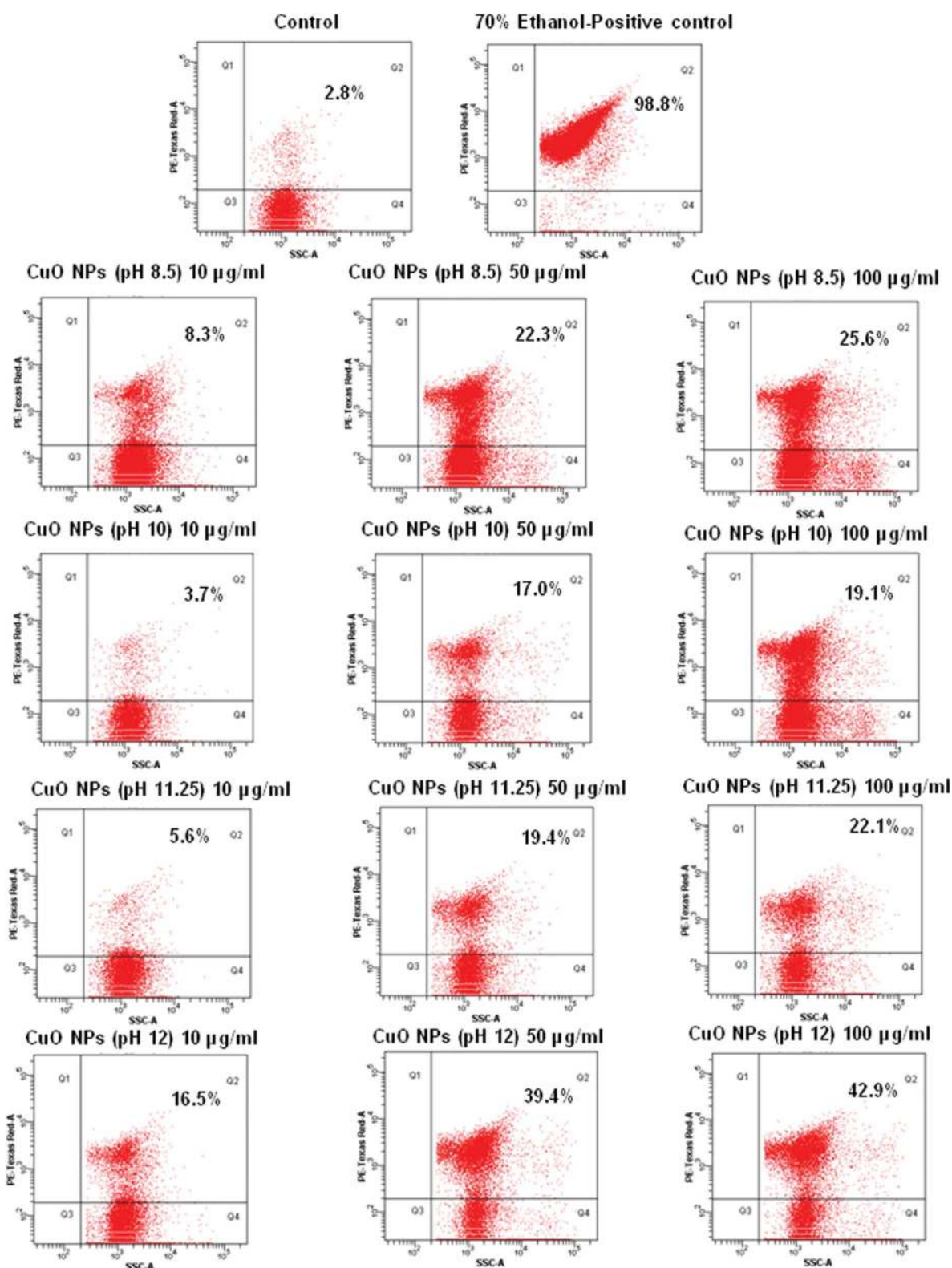


Fig. 13 Flow cytometric quantification of dead *E. coli* cells after CuO NP treatment; Q2 represents percent dead cells and Q4 represents percent live cells.

experimental error associated with our TPS-500 thermal constant analyzer is  $\pm 2\%$ .

From the figure it is visibly apparent that sample A has the most effectiveness in enhancing the TC across the whole range of experimental temperature. This sample showed an impressive TC

increment of above 40% in the temperature range of 30–70 °C. The peak at 30 °C was 48%, which is impressive considering the low volume fraction of the nanoparticles and the reported literature values for CuO nanofluids.<sup>27–29</sup> The sample B, although not as impressive as sample A, provided good results



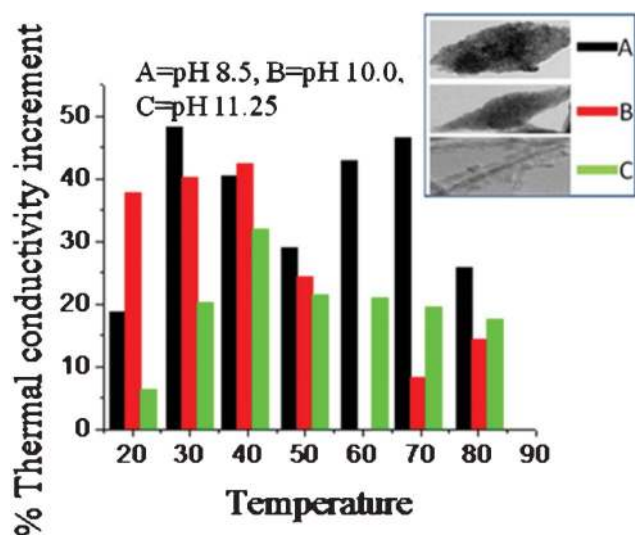


**Fig. 14** Temperature dependence of the thermal conductivity enhancement of CuO-water nanofluids prepared from different CuO nanoparticles. The synthesis pH and the corresponding shapes of the particles are provided in the inset.

nevertheless. It has a TC increment of 25–42% in the temperature region of 20–50 °C and 5–15% in the temperature region of 50–80 °C, its peak value being 42% at the temperature of 40 °C. The sample C also shows a TC increment of the base fluid in the experimental temperature region, attaining its peak at 40 °C (32%). One interesting observation here is that up to 50 °C, the nanofluid B had a higher TC increment compared to nanofluid C, but after 50 °C the trend is reversed and C produces a better TC increment compared to B.

The anomalous TC increment of the nanofluids has remained quite controversial and the proposed mechanisms behind this property have been anything but satisfying. The results have also been largely inconsistent and most of the decent results have been irreproducible. Given the inconsistency of the data published in the open literature it has so far not been possible to develop a single comprehensive and convincing physical model that can predict all the trends. The factors like size, shape, external agents, surface modulations *etc.* have all been taken into account by various researchers while interpreting their results. The effect of the particle size in modulating its properties like thermal conductivity is quite engaging in this regard. As the particle size decreases, the specific surface area of the particle increases proportionally. Heat transfer between the particle and the fluid takes place at the particle-fluid interface. Therefore, a dramatic enhancement in thermal conductivity is expected because a reduction in particle size can result in large interfacial area. Since the surface to volume ratio is much higher for the nanosized particles (1000 times, for spherical particles of 10 nm diameter compared to spherical particle of 10 μm diameter) one would expect the influence of size to be much more prominent and decreasing size of the particles to exhibit more improvement in this type of characteristic manifestations of its properties. But for our case, the results that we obtained for the three samples cannot be rationalized by the size variation of the particles. Besides, for particles that are not spherical the effect of size reduction is not that drastic and the effect of the shape can play a

crucial role. Shape dependence on the TC of two component heterogeneous systems was theoretically predicted in 1962 by Hamilton & Crosser.<sup>54</sup> Their equation regarding the thermal conductivity of a two component system is as follows

$$K = K_1 [K_2 + (n - 1) K_1 - (n - 1) V_2 (K_1 - K_2)] / [K_2 + (n - 1) K_1 + V_2 (K_1 - K_2)] \quad (4)$$

Where,  $K$  = TC of the two component system (nanofluid),  $K_1$  = TC of the continuous phase (pure water in our case),  $K_2$  = thermal conductivity of the discontinuous phase (CuO nanoparticles in our case),  $V_2$  = vol. fraction of the nanoparticles,  $n$  = empirical shape factor.  $n$  can be defined as  $n = 3/\psi$ ; where  $\psi$  = sphericity factor (*i.e.* the ratio of the surface area of a sphere having a volume equal to that of the particle, to the surface area of the particle). For spherical particles  $\psi = 3$ .

Assuming, the synthesized CuO nanoparticles are more efficient thermal conductors than water ( $K_2 \gg K_1$ ), the TC of the nanofluid can be given by the equation

$$K = K_1 [(1 + (n - 1)V_2) / (1 - V_2)] \quad (5)$$

Now the shapes of the nano CuO particles used to generate the three nanofluid samples A, B, C are seed-like, ellipsoidal and rod like respectively. The first two can be broadly categorized as prolate ellipsoids with varying axial dimensions. The ratio of height, width and thickness for them are roughly estimated from the HRTEM images to be 5 : 2 : 1 and 4 : 1 : 1 respectively for nano CuO (pH 8.5) and nano CuO (pH 10.0), whereas the ratio of height to width for the rod shaped particles were estimated to be approximately 10 : 1. The volume and the surface area of a prolate ellipsoid is given by  $V = 4/3 \times (\pi abc)$  and  $S = 4\pi\{(a^2b^p + a^2c^p + b^2c^p)/3\}^{1/p}$  respectively.

Where,  $a, b, c$  = the three axial lengths of the ellipsoid and  $p = 1.6$  for a prolate ellipsoid.

Using these equations it can be showed that for our synthesized nano CuO particles,  $\psi_A < \psi_B \ll \psi_C$ , so,  $n_A > n_B \gg n_C$ ; so, substituting them in eqn. (5) we get,  $K_A > K_B \gg K_C$ .

This is compatible with our results as the TC for sample A has produced the best increment and within the temperature range of 50 °C, the TC increment for sample B is higher than the TC increment for sample C.

Currently, there are two lines of conjecture for explaining the TC enhancement, (1) TC is enhanced by microconvection caused by the Brownian motion (BM) of the nanoparticles and (2) TC is enhanced due to the aggregation of the nanoparticles, leading to local percolation behavior. Both these explanations for TC enhancement are independent of one other. The probability of aggregation increases with decreasing particle size at a constant volume fraction because the average interparticle distance decreases, making the attractive Van der Waals force more important. Aggregation will decrease the BM due to the increase in the mass of the aggregates, whereas it can increase thermal conductivity due to percolation effects in the aggregates, as highly conducting particles touch each other in the aggregate.<sup>26</sup> From the HRTEM images of the synthesized nanoparticles (Fig. 6a,c,e) it is quite evident that these particles showed a tendency for aggregation in their dispersed state. So aggregation

may be the reason for the observed TC increment of the nanofluids. But at higher temperatures these aggregations may break down and the stochastic motion (which is dependent on the particle size) of the particles plays the dominating role in determining the TC of the nanofluids, which explains the reversal trend of the similar TC increment for sample B and C in the lower and higher temperature regions. Overall, our synthesized CuO nanoparticles demonstrate a noteworthy effect on the thermal conductivity of the base fluid water and because of their high TC in the temperature region above the room temperature, these nanofluids can be envisaged as being used in the cooling fluids of high energy density devices, since these devices mostly work at temperatures above room temperature. Besides, the nanofluids have given a positive response to the TC increment even at a very small concentration of these nanoparticles, which is very critical as a precaution against the feasible toxic effects of these particles.

## Conclusion

We have succeeded in synthesizing CuO nanomaterials by hydrolyzing  $\text{Cu}(\text{NO}_3)_2$  in an alkaline medium, followed by annealing the obtained  $\text{Cu}(\text{OH})_2$  at 130 °C. We were able to generate a variety of shapes such as seed-like, ellipsoidal, rods and leaves by simply varying the pH during the synthesis procedure. It was observed that at low pH  $\text{Cu}(\text{OH})_2$  was less stable and would convert into CuO within 10 h at room temperature. The entire process of structural inception and subsequent evolution were tracked by XRD, FT-IR, SEM and HRTEM methods. A detailed hypothesis supported by experimental evidence has been developed to account for the fascinating morphological and structural transformations that occur by changing the pH during synthesis. The optical properties of these samples were explored *via* photoluminescence spectroscopy and we found that the particles with seed-like shape possessed the most impressive luminescence and the nanorods possessed the most unusual luminescence property among the various shapes of CuO. The prepared CuO samples showed excellent responses when used as nanofluids and the thermal conductivity could be raised as high as 48%. The particles with seed-like shape were found to be the most effective in enhancing the thermal conductivity of the base fluid. The toxicity of the synthesized particles was evaluated and the leaf shaped particle was found to be comparatively more toxic than the others. Although found to be potent for causing bio-adversity, the capability of these nano CuO particles in industrial applications, even at a very low concentration, is an important finding.

## Acknowledgements

We thank the Director, NPL New Delhi, India for providing the necessary experimental facilities. Dr N. Vijayan, Dr S.N. Sharma, Mr. K.N. Sood and Mr. P. C. Mandal are gratefully acknowledged for providing the necessary instrumentation facilities for XRD, FT-IR, SEM and UV-Vis spectroscopy respectively. We also thank Dr R. Pasricha for taking part in the initial discussions. K. K. Dey acknowledges the financial support from Council of Scientific and industrial research, India (Grant No.31/001(0325/2009-EMR-I).

## References

- X. G. Zheng, H. Kubozono, H. Yamada, K. Kato, Y. Ishiwata and C. N. Xu, *Nat. Nanotechnol.*, 2008, **3**, 724–726.
- B. Gilbert, F. Huang, H. Zhang, G. A. Waychunas and J. F. Banfield, *Science*, 2004, **305**, 651–654.
- A. L. Goodwin, *Nat. Nanotechnol.*, 2008, **3**, 711–712.
- M. I. Stockman, *Nature*, 2010, **467**, 541–542.
- J. Sharma, R. Chhabra, A. Cheng, J. Brownell, Y. Liu and H. Yan, *Science*, 2009, **323**, 112–116.
- F. Carlier, S. Benrezzak, Ph. Cahuzac, N. Kebaili, A. Masson, A. K. Srivastava, C. Colliex and C. Bre'chignac, *Nano Lett.*, 2006, **6**, 1875–1879.
- M. Deepa, A. K. Srivastava, K. N. Sood and S. A. Agnihotry, *Nanotechnology*, 2006, **17**, 2625–2630.
- M. Das, C. Dhand.; G. Sumana, A. K. Srivastava, R. Nagarajan, L. Nain, M. Iwamoto, T. Manaka and B. D. Malhotra, *Biomacromolecules*, 2011, **12**, 540–547.
- S. Bhandari, M. Deepa, A. G. Joshi, A. P. Saxena and A. K. Srivastava, *Nanoscale Res. Lett.*, 2011(in press).
- A. Nel, T. Xia, L. Mädler and N. Li, *Science*, 2006, **311**, 622–627.
- T. Xia, M. Kovochich, J. Brant, M. Hotze, J. Sempf, T. Oberley, C. Sioutas, J. I. Yeh, M. R. Wiesner and A. E. Nel, *Nano Lett.*, 2006, **6**, 1794–1807.
- M. Heinlaan, A. Ivask, I. Blinova, H. C. Dubourguier and A. Kahru, *Chemosphere*, 2008, **71**, 1308–1316.
- L. Liao, Z. Zhang, B. Yan, Z. Zheng, Q. L. Bao, T. Wu, C. M. Li, Z. X. Shen, J. X. Zhang, H. Gong, J. C. Li and T. Yu, *Nanotechnology*, 2009, **20**, 085203.
- B. J. Hansen, N. Kouklin, G. Lu, I-K. Lin, J. Chen and X. Zhang, *J. Phys. Chem. C*, 2010, **114**, 2440–2447.
- J. B. Reitz and E. I. Solomon, *J. Am. Chem. Soc.*, 1998, **120**, 11467–11478.
- C. L. Carnes and K. J. Klabunde, *J. Mol. Catal. A: Chem.*, 2003, **194**, 227–236.
- J. Wang, S. He, Z. Li, X. Jing and M. Zhang, *Mater Sci-poland*, 2009, **27**, 501–507.
- J. Chen, K. Wang, L. Hartman and W. Zhou, *J. Phys. Chem. C*, 2008, **112**, 16017–16021.
- X. Gou, G. Wang, J. Yang, J. Park and D. Wexler, *J. Mater. Chem.*, 2008, **18**, 965–969.
- J. H. Schon, M. Dorget, F. C. Beuran, X. Z. Zu, E. Arushanov, C. D. Cavellin and M. Lagues, *Nature*, 2001, **414**, 434–437.
- T. Tohyama, Y. Ohta and S. Maekawa, *Phys. C*, 1989, **158**, 525–530.
- T. Maruyama, *Sol. Energy Mater. Sol. Cells*, 1998, **56**, 85–92.
- A. E. Rakhshani, *Solid-State Electron.*, 1986, **29**, 7–17.
- S. Gao, S. Yang, J. Shu, S. Zhang, Z. Li and K. Jiang, *J. Phys. Chem. C*, 2008, **112**, 19324–19328.
- S. Venkatachalam, H. Zhu, C. Masarapu, K. Hung, Z. Liu, K. Suenaga and B. Wei, *ACS Nano*, 2009, **3**, 2177–2184.
- R. Prasher, P. E. Phelan and P. Bhattacharya, *Nano Lett.*, 2006, **6**, 1529–1534.
- S. K. Das, N. Putra, P. Thiesen and W. Roetzel, *J. Heat Transfer*, 2003, **125**, 567–574.
- H. T. Zhu, C. Y. Zhang, Y. M. Tang and J. X. Wang, *J. Phys. Chem. C*, 2007, **111**, 1646–1650.
- N. R. Karthikeyan, J. Philip and B. Raj, *Mater. Chem. Phys.*, 2008, **109**, 50–55.
- X. G. Zheng, C. N. Xu, K. Nishikubo, W. J. Moon, E. Tanaka and E. S. Otake, *Phys. Rev. B: Condens. Matter Mater. Phys.*, 2005, **72**, 014464.
- X. Jiang, T. Herricks and Y. Xia, *Nano Lett.*, 2002, **2**, 1333–1338.
- J.-Y. Li, S. Xiong, J. Pan and Y. Qian, *J. Phys. Chem. C*, 2010, **114**, 9645–9650.
- C. T. Hsieh, J. M. Chen, H. H. Lin and H. C. Shih, *Appl. Phys. Lett.*, 2003, **82**, 3316–3318.
- W. Wang, Y. Zhan and G. Wang, *Chem. Commun.*, 2001, 727–728.
- L. Armelao, D. Barreca, M. Bertapelle, G. Bottaro, C. Sada and E. Tondello, *Thin Solid Films*, 2003, **442**, 48–52.
- C. Carel, M. M. Bahout and J. C. Gaude, *Solid State Ionics*, 1999, **117**, 47–55.
- C. Lu, L. Qi, J. Yang, D. Zhang, N. Wu and J. Ma, *J. Phys. Chem. B*, 2004, **108**, 17825–17831.
- W. Z. Wang, C. Lan, Y. Z. Li, K. Q. Hong and G. H. Wang, *Chem. Phys. Lett.*, 2002, **366**, 220–223.

- 39 B. X. Yang, T. R. Thurston, J. M. Tranquada and G. Shirane, *Phys. Rev. B*, 1989, **39**, 4343–4349.
- 40 X. G. Zheng, C. N. Xu, Y. Tomokiyo, E. Tanaka, H. Yamada and Y. Soejima, *Phys. Rev. Lett.*, 2000, **85**, 5170–5173.
- 41 M. Vila, C. Diaz-Guerra and J. Piqueras, *J. Phys. D: Appl. Phys.*, 2010, **43**, 135403.
- 42 S.-S. Changa, H.-J. Leea and H. J. Park, *Ceram. Int.*, 2005, **31**, 411–415.
- 43 T. Mosmann, *J. Immunol. Methods*, 1983, **65**, 55–63.
- 44 R. K. Shukla, V. Sharma, A. K. Pandey, S. Singh, S. Sultana and A. Dhawan, *Toxicol. in Vitro*, 2011, **25**, 231–241.
- 45 W. K. Jung, H. C. Koo, K. W. Kim, S. Shin, S. H. Kim and Y. H. Park, *Appl. Environ. Microbiol.*, 2008, **74**, 2171–2178.
- 46 S. H. Park and H. J. Kim, *J. Am. Chem. Soc.*, 2004, **126**, 14368–14369.
- 47 P. C. Pereira, D. L. A. D. Faria and V. R. L. Constantino, *J. Braz. Chem. Soc.*, 2006, **17**, 1651–1657.
- 48 Y. Li, 2008 *NNIN REU Research Accomplishments.*, 2008, 46–47.
- 49 A. Sambandam, W. Xiaogang and Y. Shihey, *Mater. Chem. Phys.*, 2005, **93**, 35–40.
- 50 Z. P. Zhang, H. Sun, X. Q. Shao, D. Li, H. Yu and M. Han, *Adv. Mater.*, 2005, **17**, 42–47.
- 51 A. Kumar, A. K. Pandey, S. S. Singh, R. Shanker and A. Dhawan, *Chemosphere*, 2011, **83**, 1124–1132.
- 52 H. L. Karlsson, J. Gustafsson, P. Cronholm and L. Möller, *Toxicol. Lett.*, 2009, **188**, 112–118.
- 53 P. S. Brookes, Y. Yoon, J. L. Robotham, M. W. Anders and S. S. Sheu, *Am. J. Physiol.: Cell Physiol.*, 2004, **287**, C817–C833.
- 54 R. L. Hamilton and O.K. Crosser, *I & EC Fundamentals*, 1962, **1**, 187–191.